Journal of Alloys and Compounds 1078 (2026) 189800

Contents lists available at ScienceDirect

Journal of Alloys and Compounds

journal homepage: www.elsevier.com/locate/jalcom

Tuning martensitic transformation and enhancing magnetocaloric effect in $Ni_{47}Mn_{40}Sn_{13-x}W_x$ Heusler alloy via experiments and first-principle insights

Meysam Norouzi-Inallu [a,*], Ali Ghotbi Varzaneh [b,*], Parviz Kameli [c], Ismaeil Abdolhosseini Sarsari [c], Taghi Amiri [d], Masoud Moshtaghi [a], Jingyuan Xu [b], Volodymyr Chernenko [e,f], Daniel Salazar [e], Manfred Kohl [b]

[a] Mechanics of Materials Lab, School of Energy Systems, LUT University, Lappeenranta 53850, Finland
[b] Institute of Microstructure Technology, Karlsruhe Institute of Technology, Karlsruhe 76344, Germany
[c] Department of Physics, Isfahan University of Technology, Isfahan 84156-83111, Iran
[d] Department of Chemical and Materials Engineering, University of Alberta, Edmonton, Alberta T6G 1H9, Canada
[e] BCMaterials, Basque Center for Materials, Applications and Nanostructures, EHU Science Park, Leioa 48940, Spain
[f] Ikerbasque, Basque Foundation for Science, Bilbao 48009, Spain

ARTICLE INFO

Keywords:
$Ni_{47}Mn_{40}Sn_{13-x}W_x$ metamagnetic shape memory alloys
Martensitic transformation
Magnetocaloric effect
Cyclic stability
Field-induced adiabatic temperature change
First-principle calculation

ABSTRACT

The influence of tungsten (W)-doping on the structural, magnetic, and magnetocaloric properties of $Ni_{47}Mn_{40}Sn_{13-x}W_x$ ($x = 0$, 0.5, 1, 1.25) metamagnetic shape memory alloys was investigated using a combination of experimental and first-principles methods. W-doping in Ni-Mn-Sn shifts the martensitic transformation (MT) towards room temperature and enhances the inverse magnetocaloric effect (MCE), with a maximum magnetic-field-induced entropy change of 13.2 J/kg·K at 5 T for the $x = 1$ alloy. Direct cyclic measurements at 1.96 T show stable adiabatic temperature changes ($\Delta T_{ad} \approx 0.5$ K at the MT temperature and $\Delta T_{ad} \approx 1.4$ K at the Curie temperature) over hundreds of cycles, confirming the cyclic stability. Density functional theory calculations reveal that the W-dopant increases the energy gap between the cubic and tetragonal crystal structures (from 15.8 to 43.6 meV), which correlates with the higher MT temperature observed in W-doped samples. The analysis of the total and local density of states identified W-induced enhancement of hybridization and a change in the density of states near the Fermi level, resulting in a shift of MT to room temperature and an improvement in MCE. W-doping improves the MCE properties of Ni–Mn–Sn alloys, providing a path towards energy-efficient magnetic cooling.

1. Introduction

The Ni-Mn-Z (Z = Sn, In, Sb, or Ga) based metamagnetic shape memory alloys (MetaMSMAs) have been the subject of extensive research due to their range of multifunctional properties, which are attributed to the first-order martensitic transition (FOMT) [1–9]. Particularly, previous studies have shown that variations in both the electron-to-atom (*e*/a) ratio and the unit cell volume can strongly influence the magnetic behavior of these alloys [10,11]. These variations primarily affect the magnetic moments localized on Mn atoms, which interact via the indirect Ruderman–Kittel–Kasuya–Yosida (RKKY) exchange mechanism, thereby modulating the magnitude of the magnetocaloric effect (MCE) [10,12].

Furthermore, in off-stoichiometric ($Ni_2Mn_{1+x}Z_{1-x}$) Ni–Mn–Sn Heusler-type alloys, the excess Mn atoms that occupy the Z sites (Mn_2) couple antiferromagnetically with the Mn atoms on the Mn sublattice (Mn_1), while the Mn–Mn interactions within the Mn sublattice remain predominantly ferromagnetic. This coexistence and competition between ferromagnetic (FM) and antiferromagnetic (AFM) exchange interactions are key features underlying the metamagnetic behavior of these alloys. Thus, the metamagnetic behavior in Ni–Mn–Z Heusler-type alloys is due to the Mn-rich off-stoichiometry, which plays a crucial role in modifying their magnetic and structural characteristics [13]. Furthermore, the Mn–Mn distances are incredibly sensitive to fourth-element doping, leading to a change in the magnetic interaction between and within the Mn_1- and Mn_2-sublattices in the Ni–Mn–based MetaMSMAs [1,14]. Additionally, the magnetic or nonmagnetic dopant element, which alters the 3*d*-wavefunction overlap in the Ni, Mn, and

* Corresponding authors.
E-mail addresses: meysam.norouzi.inallu@lut.fi (M. Norouzi-Inallu), ali.ghotbi@kit.edu (A.G. Varzaneh).

https://doi.org/10.1016/j.jallcom.2026.189800
Received 30 April 2026; Received in revised form 9 July 2026; Accepted 11 July 2026
Available online 13 July 2026

the Z = Sn, In, and Ga sites, can significantly affect RKKY interactions and magnetostructural stability [15–17].

Foremost, the significant improvement of MCE in Ni-Mn-Z Meta-MSMAs involves tailoring structural and magnetic properties by doping a fourth element via partial substitution at different crystal lattice sites. This type of doping has a significant effect on the electronic structure and magnetic interactions, resulting in a complex interplay between the crystal lattice, magnetization, and electron transport during MT [4,18]. Previous reports suggest that the magnetic contribution to the overall entropy change (between different degrees of freedom in the crystal lattice, including magnetic, electronic systems, and orderings) is a primary factor in the MCE effect owing to MT [19,20]. Therefore, the magnetocaloric properties can be practically adjusted by doping Meta-MSMAs with either magnetic or nonmagnetic elements [21–23].

Despite extensive research on lighter dopants and magnetic elements, the potential of 5*d* transition metals, such as tungsten (W), has been explored relatively rarely. This knowledge gap limits our understanding of how the incorporation of nonmagnetic W modifies the electronic structure, magnetic exchange interactions, and transformation behavior in Ni–Mn–Sn Heusler-type alloys. Beyond conventional doping strategies that primarily tune the valence electron concentration (*e*/a), replacing Sn(5*p*) with W(5*d*) introduces more spatially extended orbitals and a different hybridization environment, which can modify the electronic states near the Fermi level and influence the relative stability of competing phases.

This work combines comprehensive experimental characterization with first-principles calculations to clarify the role of W-doping at Sn sites in Ni–Mn–Sn Heusler-type alloys. The first-principle results consistently predict the experimentally observed increase in the MT temperature upon W-doping. Furthermore, the calculations reveal an increased energy difference between the cubic and tetragonal phases, suggesting that the observed MT shift is associated not only with *e*/a modification but also with W-induced changes in electronic structure and lattice stability. Moreover, we examine the cyclic performance of both the inverse and conventional magnetocaloric effects across MT and the Curie temperature, demonstrating stable behavior under repeated magnetic-field cycling. Although the achieved MCE is not the highest among Ni–Mn–X systems, the present study demonstrates a balanced optimization of room-temperature transformation, entropy change, and cyclic stability. In addition, the W-induced modification of orbital hybridization may strengthen interatomic bonding, which is relevant for improving the mechanical robustness required in future multicaloric applications [24]. These findings highlight the relatively unexplored role of 5*d*-element substitution as a reliable approach for tailoring magnetostructural properties while maintaining reversible and durable magnetocaloric functionality.

2. Materials and methods

2.1. Experimental details

$Ni_{47}Mn_{40}Sn_{13-x}W_x$ (x= 0, 0.5, 1, and 1.25) alloys were prepared by mechanical alloying, as described elsewhere [21,25]. The crystal structures were monitored by X-ray diffraction (XRD, ASENWARE AW-DX300) using Cu-Kα radiation (λ= 1.54184 Å, 40 kV, 30 mA) at room temperature. All magnetization measurements were conducted with a SQUID magnetometer (Quantum Design, MPMS3) up to 5 T. Direct measurements of ΔT_{ad} for a magnetic field change of 1.96 T were performed using a homemade adiabatic calorimeter described elsewhere [26]. The actual compositions of the alloys were determined using a Hitachi TM3000 scanning electron microscope equipped with an energy-dispersive X-ray spectroscopy (EDS) system.

2.2. Computational details

Electronic structure calculations were conducted with plane-wave-based Density Functional Theory (DFT) implemented in the QUANTUM ESPRESSO package at zero temperature [27]. The projector augmented wave (PAW) pseudo-potentials method was used with the following valence electron configurations: Ni ($4s^2 3d^8 4p^0$), Mn ($3p^6 4s^2 3d^5$), Sn ($5s^2 4d^{10} 5p^2$), and W ($5d^4 6s^2 6p^0$). For DFT calculations, all pseudopotentials were obtained from the PS library 0.3.1, using the Perdew-Burke-Ernzerhof (PBE) exchange-correlation functional [28]. The nonstoichiometric compositions were treated using the supercell approach. The $Ni_8Mn_6Sn_2$ and $Ni_{16}Mn_{12}Sn_3W_1$ supercells, containing 16 and 32 atoms, respectively, were generated using VESTA and used to represent the undoped alloy and a nominal W-doping concentration of 3.125% [1,29]. Although the 32-atom supercell corresponds to a higher nominal W concentration (3.125 at%) than the experimental alloys, a 64-atom supercell with 1.5625 at% W was also tested and showed essentially the same trends in lattice parameter and magnetic moments; therefore, the 32-atom model was used mainly to discuss qualitative trends and mechanisms. The energy dependence on the tetragonality ratio, $E(c/a)$, was first obtained by relaxing the atomic positions while keeping the unit cell volume fixed at the equilibrium volume of the cubic structure. Subsequently, full structural relaxation, including both atomic positions and lattice vectors, was carried out only for selected c/a values corresponding to the energy minima. Thus, the unit cell volume was reoptimized only at the minimum-energy configurations [1].

3. Results and discussion

3.1. Structural properties

Table 1 lists the actual alloy compositions determined by EDS with an uncertainty of 0.5 at%, which closely matches the nominal values, and the *e*/a was calculated accordingly. XRD patterns at room temperature confirm the presence of a Heusler-type $L2_1$-ordered cubic austenitic phase (*Fm-3m* space group) for $x = 0$, 0.5, and 1, evidenced by (111) and (200) superlattice peaks in Fig. 1 [30,31]. A trace of martensite is observed in the $x = 1$ sample, likely due to proximity to the transformation temperature [21,32]. At $x = 1.25$, the martensitic phase with orthorhombic structure (*Pmma* space group) becomes dominant, with residual austenite indicating that the structural transition may take place at higher temperatures than samples with lower amounts of W-doping [30–34]. Additionally, the low χ^2 values indicate good agreement between the experimental XRD data and the fitted structural models.

As shown in Table 1, increasing the W content reduces the lattice parameters, which may be attributed to the replacement of larger Sn atoms (1.40 Å) with slightly smaller W atoms (1.39 Å). However, the reduction in lattice parameters observed with W-doping cannot be explained solely by the minor difference in atomic radii between Sn and W. Rather, this phenomenon is governed by multiple factors, including alterations in the electronic structure resulting from changes in the *e*/a ratio, and variations in atomic disorder and site occupancy. Furthermore, microstructural effects such as internal stresses and local compositional inhomogeneities may also contribute to the observed lattice contraction [11,33]. Furthermore, the pseudo-cubic lattice parameter (a_{pc}) was calculated using the relation $a_{pc} = \left(\frac{V}{n}\right)^{1/3} = \left(\frac{a\times b\times c}{n}\right)^{1/3}$, where V is the unit cell volume, and n is the number of formula units per unit cell. This definition enables direct comparison of equivalent atomic volumes between the cubic austenitic phase ($n = 4$) and the orthorhombic martensitic phase. For consistency, $n = 4$ was adopted for both phases, in agreement with commonly reported crystallographic descriptions of Ni–Mn–based Heusler alloys. The moderate reduction in a_{pc} values with increasing W content (Table 1) suggests that the observed lattice contraction may be driven by atomic substitution, with contributions from electronic-state effects and structural

Table 1
Actual chemical compositions (in at%), electron-to-atom concentration (e/a), lattice parameters, χ^2 values, unit cell volume, and pseudo-cubic lattice parameter (a_{pc}), of the $Ni_{47}Mn_{40}Sn_{13-x}W_x$ ($x = 0$, 0.5, 1, and 1.25 at%) alloys. All lattice constants are presented with an approximate accuracy of ±0.005 Å.

Alloy	Compositions (at% ± 0.5)				e/a (-)	Crystal structure at room temperature			
	Ni	Mn	Sn	W		Lattice parameter (Å)	χ^2 (-)	Unit cell volume (Å)^3	a_{pc} (Å)
$x = 0$	47	40.2	12.8	-	8.020	$a = 5.993$	1.09	215.245	4.238
$x = 0.5$	47.2	40.1	12.5	0.2	8.030	$a = 5.985$	1.14	214.384	4.232
$x = 1$	47.1	39.8	12.5	0.6	8.040	$a = 5.981$	1.19	213.955	4.229
$x = 1.25$	47.2	40.3	11.3	1.3	8.045	$a = 8.494$, $b = 5.715$, $c = 4.319$	1.39	209.658	3.742

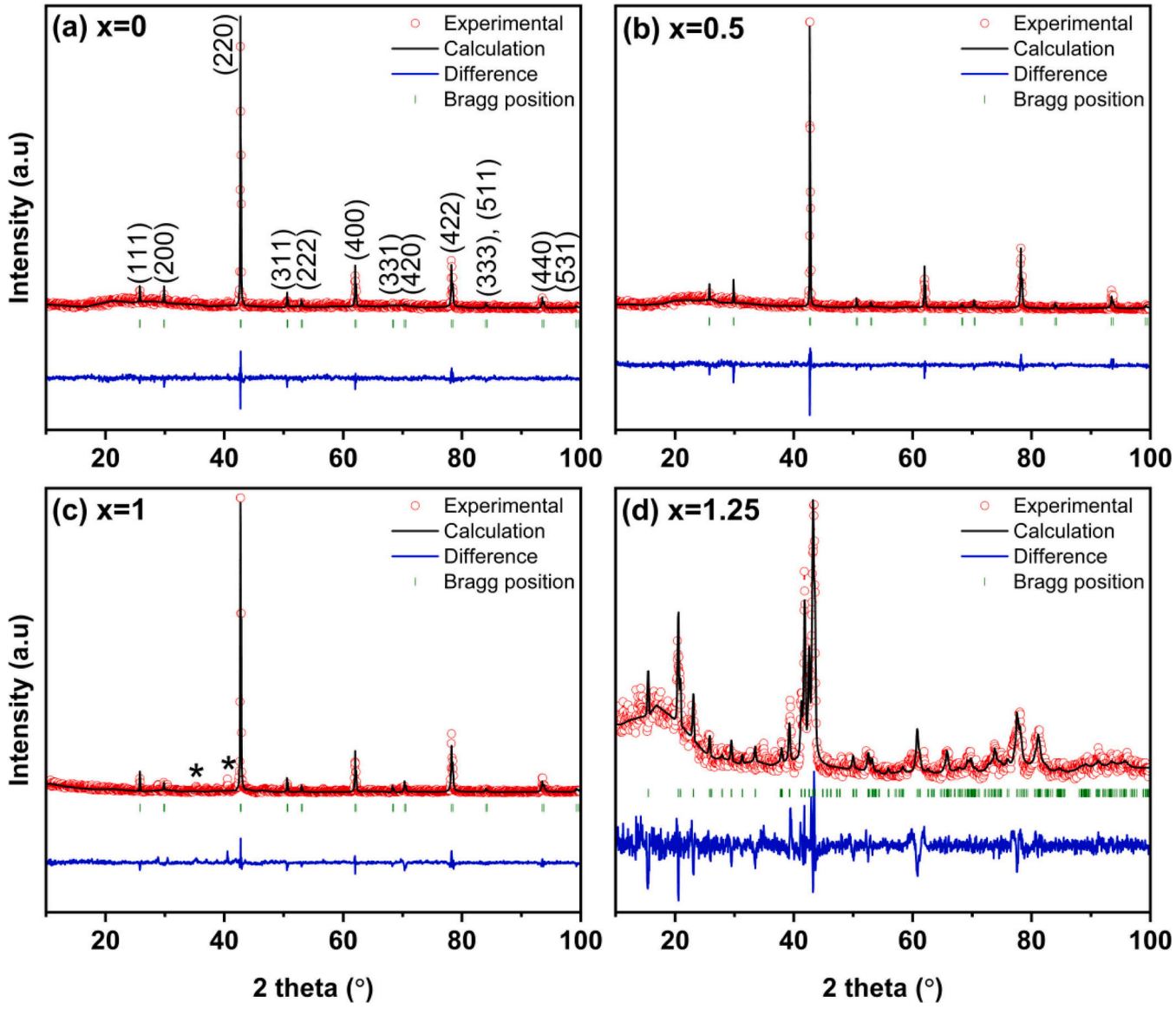

Fig. 1. Rietveld refinement of X-ray diffraction patterns for $Ni_{47}Mn_{40}Sn_{13-x}W_x$ alloys, where $x = 0$ (a), 0.5 (b), 1 (c), and 1.25 (d) at room temperature. The red circles indicate the observed counts, and the black line represents the calculated values. Blue lines correspond to the difference between the calculated and observed patterns. Green vertical bars show the Bragg positions.

modifications.

3.2. Magnetic and magnetocaloric properties

Fig. 2 shows the thermomagnetization curves, $M(T)$, for $Ni_{47}Mn_{40}Sn_{13-x}W_x$ ($x = 0$, 0.5, 1, and 1.25) alloys under different magnetic fields from 0.1 to 5 T. Magnetic transformation occurs from paramagnetic to FM state at the Curie temperature (T_C). The samples exhibit a FOMT, with a sudden magnetization jump (ΔM), at the martensitic $\left(T_M = \left(T_M^s + T_M^f\right)/2\right)$ and austenitic $\left(T_A = \left(T_A^s + T_A^f\right)/2\right)$ transformation temperatures. The insets of Fig. 2 show that the W dopant influences the Ni-Mn-Sn-based MetaMSMAs' response to an applied magnetic field. The transition temperature of the MT decreases with the magnetic field at a rate of −1.27, −1.06, −0.51, and −0.46 K/T in $Ni_{47}Mn_{40}Sn_{13-x}W_x$ ($x = 0$, 0.5, 1, and 1.25) alloys, respectively. The value of the thermal hysteresis shift is considered an important

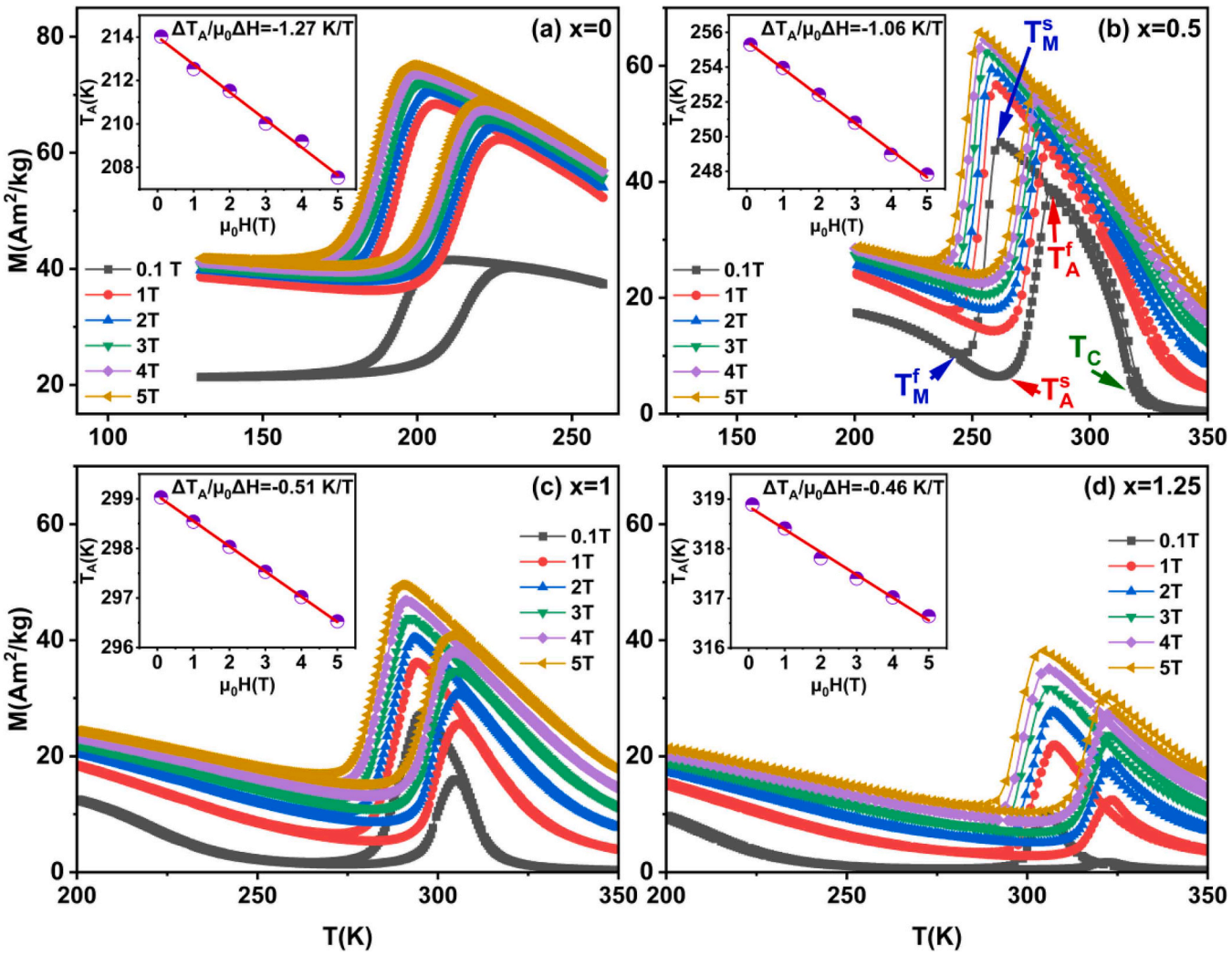

Fig. 2. (a-d) Thermomagnetization curves, $M(T)$, for $Ni_{47}Mn_{40}Sn_{13-x}W_x$ alloys ($x = 0$, $x = 0.5$, $x = 1$, and $x = 1.25$ at%) measured under different magnetic fields in the range of 0.1 T - 5 T. The martensitic start and finish temperatures, (T_M^s) and $\left(T_M^f\right)$, austenitic start and finish temperatures, (T_A^s) and $\left(T_A^f\right)$, the Curie temperature (T_C) are shown in the (b) panel. The Insets show the shift of the austenitic $\left(T_A = \left(T_A^s + T_A^f\right)/2\right)$ transformation temperatures as a function of applied magnetic field.

parameter controlling the temperature-magnetic field window for magnetocaloric operations and applications, and higher rates of the magnetic-field-induced shift of transition temperature ($\Delta T_A/\mu_0\Delta H$) indicate that a higher volume fraction of the martensite phase is converted to the austenite phase at a lower applied magnetic field [35,36].

Fig. 3 shows the magnetic entropy change (ΔS_{iso}) as a function of temperature under different magnetic fields that were determined using the data from Fig. 1 and applying the thermodynamic Maxwell relationship, represented by Eq. 1 [21]:

$$\Delta S_{iso}(T_j, \Delta H) = \sum_{i=1}^{n-1}\left[\left(\frac{\partial M_i}{\partial T_j}\right)_{H_i} + \left(\frac{\partial M_{i+1}}{\partial T_j}\right)_{H_{i+1}}\right] \times \left[\frac{\Delta H}{2}\right] \quad (1)$$

where M_i and M_{i+1} indicate the magnetization values at applied magnetic field H_i and H_{i+1}, respectively, and temperature T_j; ΔH represents the incremental change in the magnetic field between distinct thermomagnetic curves.

As seen in Fig. 3(a), the $x = 0$ sample exhibits a relatively small ΔS_{iso} peak near the MT, consistent with the weak magnetization difference between the austenite and martensite phases. The ΔS_{iso} peak increases noticeably and shifts to higher temperatures with the addition of W ($x = 0.5$), reflecting enhanced magnetostructural coupling and a larger ΔM across the transformation. The sample with $x = 1$ shows the highest ΔS_{iso} values at all applied magnetic fields, reaching its maximum of about 13.2 J/kg·K at 5 T (see Fig. 3(c)). This enhancement originates from the large magnetization jump at the martensitic transition, which facilitates a more effective field-induced conversion between martensite and austenite. Applying higher magnetic fields increases the fraction of the martensitic phase converted to austenite, leading to a larger inverse MCE at higher fields [12]. This behavior highlights the interplay between the ΔM and the field-induced shift of the MT temperature. While a significant ΔM enhances the magnetocaloric effect by promoting a strong magnetostructural coupling, it also increases the magnetic entropy contribution, which opposes the lattice entropy change. Therefore, an optimal balance between ΔM and $\Delta T_A/\mu_0\Delta H$ is essential for maximizing the total entropy change.

The magnetocaloric response does not increase indefinitely with ΔM or field strength. Initially, the entropy change increases because a larger portion of martensite transforms into austenite under the applied field. However, beyond a certain point, increasing ΔM or the field strength led to decreasing returns. This occurs because the opposing magnetic entropy contribution becomes significant. As a result, the magnetocaloric effect reaches a peak and then declines, reflecting the intrinsic trade-off between structural and magnetic entropy contributions in inverse MCE systems [36,37]. For $x = 1.25$ (see Fig. 3(d)), the ΔS_{iso} peak decreases again despite the transformation occurring at higher temperatures. This reduction is attributed to the weaker ferromagnetic order in the

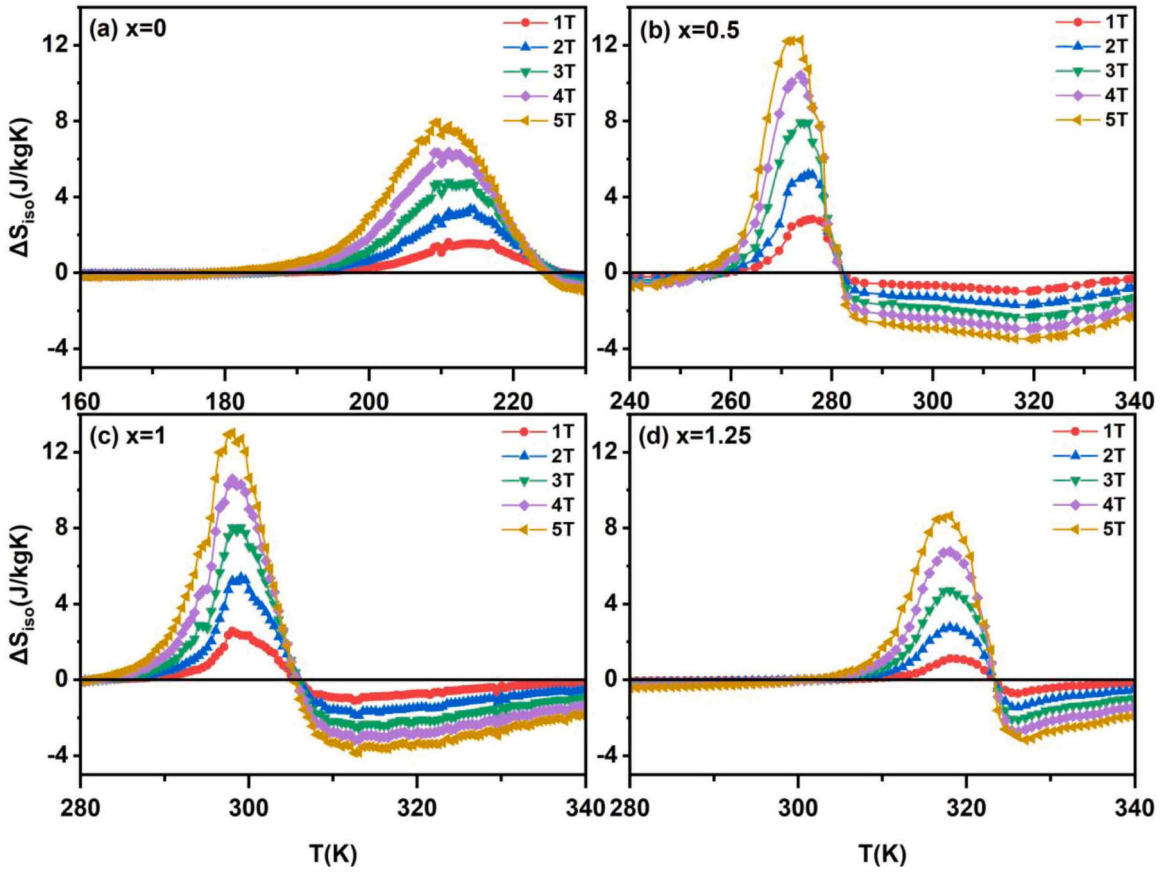

Fig. 3. Temperature dependences of the magnetic entropy change (ΔS_{iso}) as a function of temperature under different magnetic fields for $Ni_{47}Mn_{40}Sn_{13-x}W_x$ alloys, where $x = 0$ (a), $x = 0.5$ (b), $x = 1$ (c), and $x = 1.25$ (d) at%.

austenite phase at the onset of the transformation, which lowers ΔM and consequently diminishes ΔS_{iso}. This trend is consistent with the role of Zeeman energy, which depends on the magnetization contrast between the two phases [22].

Overall, increasing W-doping shifts the MT to higher temperatures, accompanied by a reduction in the $T_C - T_M^s$. A smaller value of this parameter diminishes the spin-alignment effect and enables higher achievable total entropy changes [23,38]. Additionally, W-doping modifies the hysteresis width (ΔT_{hys}), as shown in Fig. 4(a). A decrease in ΔT_{hys} with increasing W content reduces energy loss and improves cycling performance.

Based on the Clausius-Clapeyron relationship, Eq. 2 [23]:

$$\frac{\Delta T_A}{\mu_0 \Delta H} = -\frac{\Delta M}{\Delta S_{tr}} \tag{2}$$

A smaller value of the $\Delta T_A/\mu_0\Delta H$ shift corresponds to a more

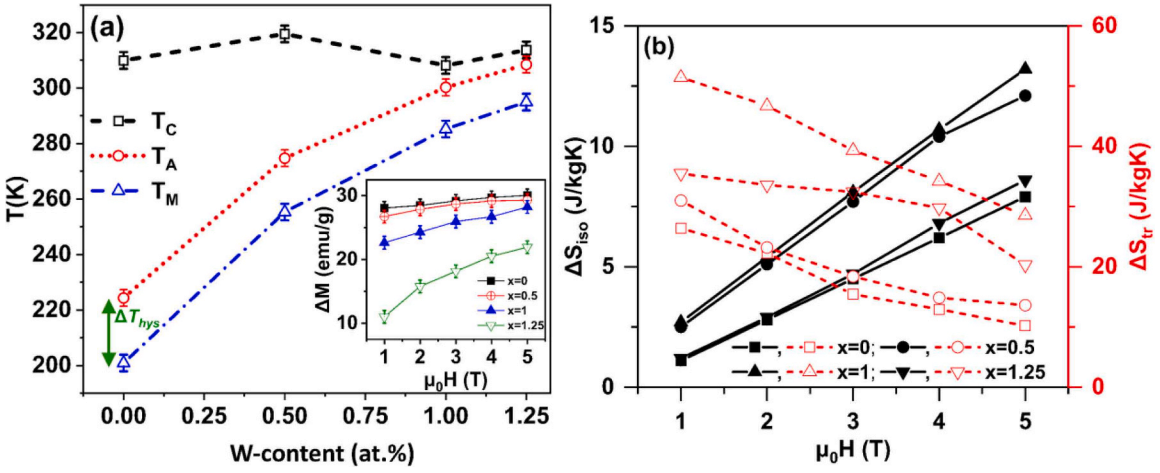

Fig. 4. (a) The martensitic (T_M) and austenitic (T_A) transformation temperatures and Curie temperature (T_C) as a function of the W content x at 0.1 T and calculated electron-to-atom ratio (e/a) for $Ni_{47}Mn_{40}Sn_{13-x}W_x$ ($x = 0$, 0.5, 1, and 1.25 at%) alloys. The green double arrow indicates the hysteresis width of MT (ΔT_{hys}). The inset shows the magnetization jumps (ΔM) across the reverse MT. (b) The ΔS_{tr} values were evaluated by the Clausius-Clapeyron relationship. The maximum values of ΔS_{iso} were calculated by the Maxwell relationship.

considerable value of structural contribution (ΔS_{tr}) to the total isothermal entropy change (at fixed ΔM), which is confirmed by the results observed for W-doped samples. This indirect thermodynamic approach has been widely employed in previous studies [39,40] for first-order magnetocaloric materials, as it reliably correlates the $\Delta T_A/\mu_0\Delta H$ with the ΔM. Xu et al. [40] demonstrated that the Clausius–Clapeyron (CC)-based method provides an accurate and physically meaningful estimate of the isothermal entropy change (ΔS_{iso}) in first-order magnetocaloric materials. This approach explicitly accounts for the phase fraction during the structural transition, thereby improving on the conventional Maxwell relation (MR). The CC-based method produces ΔS_{iso} values that closely match those obtained from MR using magnetic measurements for several Heusler alloys, while requiring a limited number of thermomagnetic curves. In contrast, MR derived from isothermal magnetization measurements may introduce artificial spikes due to hysteresis, leading to an overestimation of ΔS_{iso}. Consequently, the CC-based method is more reliable and convenient, particularly for systems with strong first-order transitions and magnetic hysteresis.

The inset of Fig. 4(a) shows that samples exhibit almost the same value of ΔM at high fields, but the MT shift for $x = 1$ is smaller than the one for $x = 0.5$. It appears that the competition between these two parameters results in larger entropy changes in the x=1 sample. Fig. 4(b) shows that increasing the magnetic field results in a moderate decrease in ΔS_{tr}, due to a reduction in the ΔS_{iso} contribution to the total entropy of the sample, caused by the alignment of magnetic moments under the influence of an applied magnetic field [42,43]. The values of ΔS_{iso} obtained in the present work at a field of about 5 T are considerable and are listed in Table 2, together with those reported in the literature for similar Ni-Mn-Sn-based MetaMSMAs.

MCE results from the thermomagnetization measurement show relatively high ΔS_{iso} values for the $x = 1$ alloy, indicating that it is a promising material for room-temperature magnetic refrigeration. The earlier results also indicated that the direct field-induced adiabatic temperature change (ΔT_{ad}) of the $x = 1$ alloy was 1.1 K at FOMT, measured using an adiabatic magneto-calorimeter [21]. Gamzatov et al. [36] investigated an inverse–direct MCE crossover in $Ni_{47}Mn_{40}Sn_{12.5}Cu_{0.5}$ Heusler-type alloys during cyclic magnetic field application. However, the inverse MCE observed in the first cycle gradually diminished with subsequent cycles and disappeared after fewer than 10 cycles, leaving only the conventional direct MCE response. This behavior was attributed to the irreversible martensite–austenite transformation within the temperature hysteresis loop, which prevents full reversibility at 1.8 T. Kamantsev et al. [44] performed multiple cycles in $Ni_{47}Mn_{40}Sn_{12.5}Cu_{0.5}$ Heusler-type alloy and confirmed that the crossover occurs rapidly, with the inverse effect disappearing after approximately 7 cycles. Gamzatov et al. [45] also examined the frequency dependence of ΔT_{ad} in $Ni_{50}Mn_{28}Ga_{22-x}(Cu, Zn)_x$ alloys under cyclic magnetic fields (0.62 and 1.2 T) at frequencies up to 20 Hz. They reported that the $Ni_{50}Mn_{28}Ga_{22}$ alloy exhibited ΔT_{ad} values of 0.74 K at 1 Hz and 0.40 K at 20 Hz in a 1.2 T field. In addition, Cu/Zn-doped significantly reduced ΔT_{ad} values and enhanced their frequency dependence. This effect was attributed to microstructural inhomogeneity and martensite–austenite phase coexistence, which increases magnetic viscosity and thermal relaxation times, thereby limiting reversibility under dynamic conditions.

In the present study, the $x = 1$ alloy with low thermal hysteresis was used to determine precisely the number of cyclic stabilities of ΔT_{ad}. Therefore, the cycling measurement was conducted at constant temperatures by inserting/removing the applied magnetic field of 1.96 T, with a complete cycle time of 5 s, as reported earlier [46,47]. Fig. 5 presents the directly measured cyclic adiabatic temperature change of this sample near the FOMT during heating. The temperature oscillations reveal the inverse magnetocaloric effect value of approximately 0.5 K during FOMT. The first cycle exhibits the largest ΔT_{ad}, followed by a slight reduction, after which the amplitude stabilizes over several cycles. Notably, the slight heating observed during cyclic measurements results from unavoidable heat transfer from the surroundings into the sample, thereby preventing perfectly adiabatic conditions.

Fig. 5 shows that, for the FOMT in the $x = 1$ alloy, the reduction factor of ΔT_{ad} after the initial magnetic-field cycle is relatively small and significantly lower than the typical 2.5-fold decrease reported for other Ni–Mn-based Heusler-type alloys [36,48]. During subsequent magnetic-field cycles, the maximum ΔT_{ad} remains nearly constant, confirming the cyclic stability of the x = 1 alloy. This stable performance aligns with previous reports on Ni–Mn–based MetaMSMAs [46,49], which also display consistently high ΔM values and a narrower thermal hysteresis. Notably, the moderate upward drift observed during extended cycling likely results from the limited temperature stability of the experimental setup at temperatures below room temperature.

Following the initial cyclic stability behavior at FOMT, subsequent cycles exhibit reproducible oscillations, with amplitude stabilization occurring within 5–10 cycles, independent of the thermal protocol used. In this work, more than 200 s were conducted at an MT temperature higher than that reported in typical studies of similar Ni–Mn–based MetaMSMAs, thereby demonstrating the $x = 1$ alloy's good long-term cyclic stability. Once a steady state of periodic ΔT_{ad} is established, the magnetocaloric response becomes nearly identical for both direct and reverse MTs, confirming the highly reversible nature of the magnetic-field-induced phase transition.

Furthermore, the cyclic magnetocaloric response was evaluated near the Curie temperature (T_C) to assess its stability under repeated

Table 2
Parameters of the maximum on the ΔS_{iso} versus temperature curve characterizing the inverse MCE under the field of 5 T for the undoped and W-doped Ni-Mn-Sn alloys obtained in the present work, compared to the literature results for similar Ni-Mn-Sn-based MetaMSMAs.

Alloys	T (K)	ΔS_{iso} (J/kg K)	Ref.
$Ni_{47}Mn_{40}Sn_{13}$	209	7.9	This work
$Ni_{47}Mn_{40}Sn_{12.5}W_{0.5}$	273	12.1	This work
$Ni_{47}Mn_{40}Sn_{12}W_1$	298	13.2	This work
$Ni_{47}Mn_{40}Sn_{11.75}W_{1.25}$	317	8.6	This work
$Ni_{47}Mn_{40}Sn_{12}Zn_1$	270	16.0	[1]
$Ni_{48}Mn_{39}Sn_{12}Si_1$	200	5.1	[2]
$Ni_{47}Mn_{40}Sn_{12}Cd_1$	292	12.5	[12]
$Ni_{42}Fe_8Mn_{40}Sn_{10}$	280	11.0	[19]
$Ni_{47}Mn_{40}Sn_{12}Cu_1$	296	15.6	[30]
$Ni_{45}Mn_{44}Sn_8In_3$	308.5	11.2	[41]

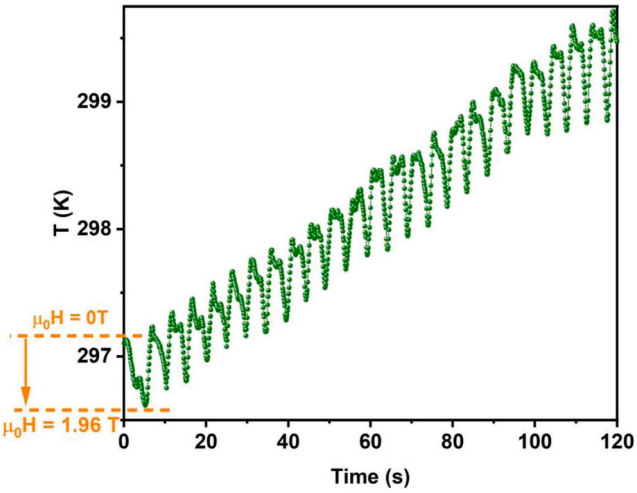

Fig. 5. Time dependence of the cyclical magnetic field induced adiabatic temperature change across the reverse MT for the $x = 1$ alloy under a magnetic field of 1.96 T at 296 K during 24 cycles.

magnetic-field variations. Fig. 6(a) shows the thermal response of the $x = 1$ alloy at two temperatures (306 K and 315 K) over 1400 s near the second-order magnetic phase transition (SOMT). The observed oscillatory profiles demonstrate dynamic magnetocaloric behavior as the magnetic field is alternately applied and removed.

After several cycles, the system attains a steady state, suggesting that the magnetic field suppresses thermal fluctuations and facilitates equilibrium during cycling. This observation is consistent with the reversible nature of magnetocaloric effects near SOMT, where the entropy change is controlled by magnetic ordering rather than structural transformation [4,50]. The lack of significant drift after multiple cycles confirms the stability of ΔT_{ad} in this regime, in agreement with previous findings in Ni–Mn–In–Ga alloys [49]. The estimated ΔT_{ad} values from Fig. 6(b) are approximately 1.4 K at 306 K and from Fig. 6(c) are approximately 1.2 K at 315 K, indicating a moderate magnetocaloric response near SOMT. Although ΔS_{iso} near the inverse MT is larger than that near T_C, the measured ΔT_{ad} values are comparable. This may be related to the sharpness of the MT and its proximity to T_C, where small temperature fluctuations during stabilization can partially transform the sample before field cycling, reducing the available transformable fraction. Differences in effective heat capacity near the two transitions may also contribute to the non-proportional relation between ΔS_{iso} and ΔT_{ad}. This results in the reproducibility of ΔT_{ad} under both SOMT and FOMT conditions in W-doped Ni–Mn–Sn alloys, comparable to that in previously reported Ga-doped Ni–Mn–In alloys [47] for long-term functional applications such as magnetic refrigeration. Notably, the slight heating

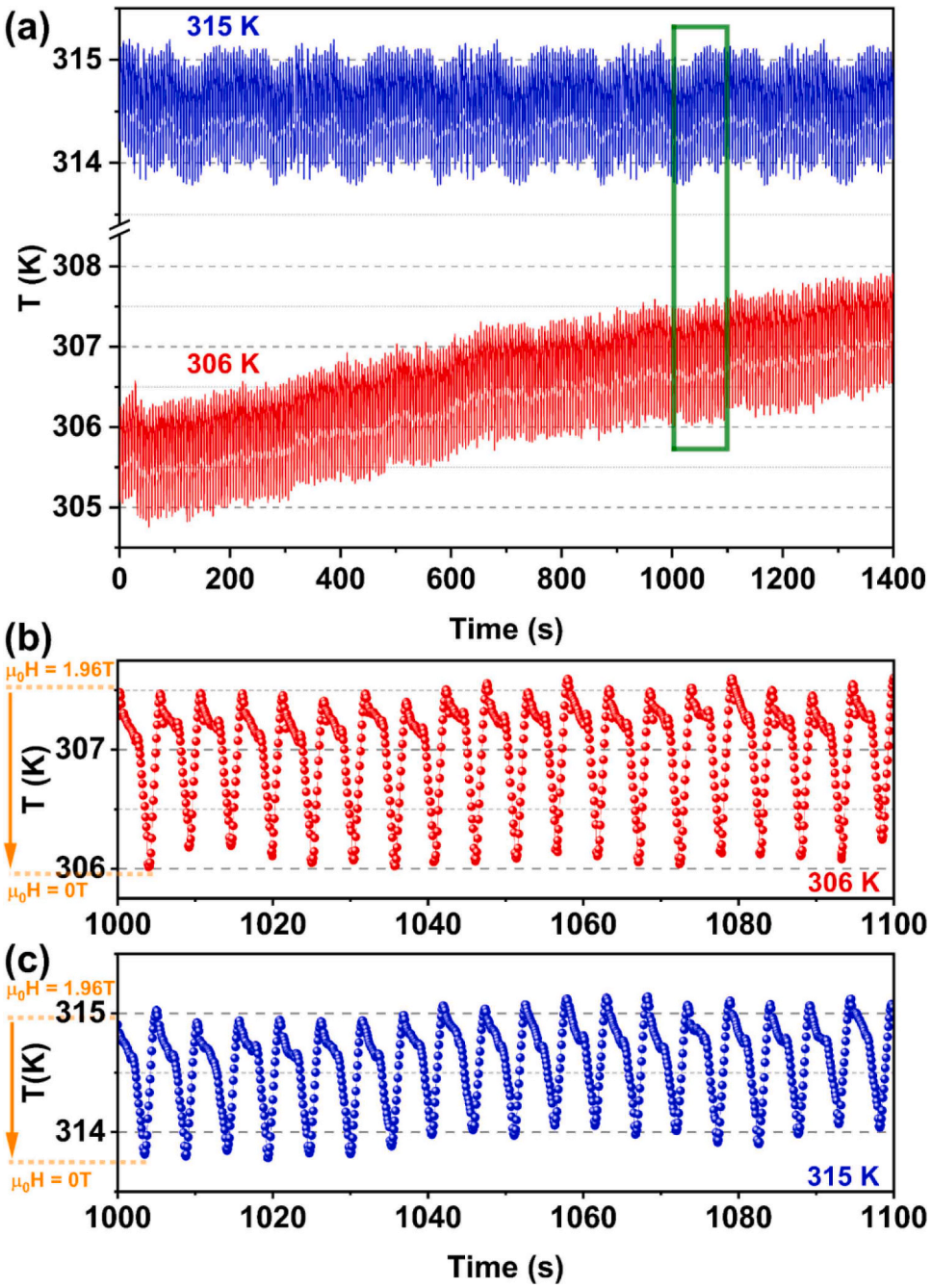

Fig. 6. Time dependences of the cyclic stability of the field-induced adiabatic temperature change for $x = 1$ alloy at 306 K (around reverse MT temperature), and at 315 K (near the second-order ferromagnetic transition) upon the cyclical variation of the magnetic field during 280 cycles (a). Enlarged views of the cyclic behavior during the time period between 1000 and 1100 s are marked in (a) by a green box (b, c).

observed during cyclic measurements is due to unavoidable heat transfer from the surroundings, making perfectly adiabatic conditions impossible.

3.3. Computational results

A theoretical study was conducted to better understand the impact of the W dopant on the magnetic properties of Ni-Mn-Sn Heusler-type alloys. This study used first-principles computations with the supercell approach, as described in earlier investigations [1,12]. The total energy is computed by relaxing the atomic positions while keeping the unit cell volume of the cubic structure ($V = a^3$) constant as a function of the tetragonality ratio c/a. Next, the minimum energies were studied for specific values of c/a in the fully relaxed state, including atomic positions and unit cell volume [12,51]. Fig. 7 illustrates the total-energy evolution of the $Ni_{16}Mn_{12}Sn_{4-x}W_x$ compound ($x = 0$ and 1) under tetragonal distortion of the optimized $L2_1$ structure, used to examine the driving forces for MT and the influence of W-doping.

The calculations were performed for both parallel (P) and antiparallel (AP) magnetic configurations, corresponding to ferromagnetic (FM) and antiferromagnetic (AFM) alignments, respectively. In the FM configuration, the magnetic moments of Mn_1–Mn_1, Ni–Mn_1, and Mn_1–Mn_2 atomic pairs are aligned parallel. In contrast, the AFM configuration refers to the antiparallel alignment between Mn_1 and Mn_2 moments, as depicted in Fig. 7. The total energy (per formula unit) relative to the cubic phase with antiparallel alignment as a function of the tetragonal distortions (c/a, c along the z-axis) has been calculated. The resulting energy curves reveal that the AFM state is favored energetically for the entire range of c/a ratios, which means that the Mn_1 and Mn_2 magnetic interactions in both austenite and martensite are antiparallel alignment, leading to a decrease in ferromagnetic exchange coupling [1,52]. It should be noted that the calculated AFM configuration corresponds to antiparallel Mn_1–Mn_2 moments within a mixed FM/AFM magnetic background rather than a fully antiferromagnetic state. Although this configuration is energetically favored at 0 K, the experimental austenite phase exhibits ferromagnetic/ferrimagnetic behavior below T_C. Similar discrepancies have been reported previously for Ni–Mn–Sn-based alloys [1,53] and are likely related to the small energy difference between competing magnetic states and the approximations inherent in standard DFT calculations. In such cases, including on-site Coulomb interactions through a Hubbard U correction may improve the description of the relative stability of closely competing magnetic configurations.

Furthermore, the differences in formation energy ($\Delta E = E_{AP}^{Cub.} - E_{AP}^{Tetra.}$) between the two magnetic phases is calculated [54], and ΔE for $Ni_8Mn_6Sn_2$ and $Ni_{16}Mn_{12}Sn_3W_1$ compounds are 15.824 meV and 43.636 meV, respectively. Since phase stability can be assessed through the formation of energy, the magnitude of ΔE plays a critical role in determining the MT characteristics [1,17].

In terms of energy stability, the MT temperature can be qualitatively estimated from the depth of the tetragonality energy valley, owing to the correlation between energy and transformation temperature ($E \approx k_BT$) [12]. A larger ΔE corresponds to a deeper tetragonal minimum and thus indicates a higher probability for the occurrence of the structural transformation, along with a more stable tetragonal phase. In the present case, W-doping significantly increases ΔE, implying enhanced stabilization of the tetragonal martensitic structure and a corresponding rise in the MT temperature. This trend is fully consistent with our experimental observations. Applying the concept to the present study shows that differences in the crystal lattices between the martensite and austenite phases lead to changes in the band structure and density of states near the Fermi level (E_F) [51,55]. The computed equilibrium lattice constants for the AFM configuration cubic phase are 6.034 Å and 6.004 Å for the undoped and W-doped alloys, respectively, in good agreement with the experimentally observed trend of decreasing lattice parameter upon W substitution. More generally, the MT temperature is known to correlate with variations in the lattice parameter induced by compositional tuning and/or the introduction of a fourth-element dopant [1,33]. In this context, replacing Sn atoms (1.40 Å) with slightly smaller W atoms (1.39 Å) leads to lattice contraction and a reduced unit cell volume, which in turn modifies the electronic density of states near the Fermi level, alters orbital hybridization, and contributes to an increase in the MT temperature [56].

Fig. 8 presents the spin-resolved total and local density of states (LDOS) for undoped and W-doped Ni–Mn–Sn Heusler-type alloys in both cubic and tetragonal phases. In the cubic austenite state of the undoped compound (Fig. 8(a)), a pronounced Ni-derived peak appears near the E_F, indicating electronic instability characteristic of high-symmetry structures. Following the transition from cubic to tetragonal, this peak splits into two distinct features, one below and one above the Fermi level (see Fig. 8(b)), indicating the Jahn–Teller effect, which stabilizes the tetragonal phase by lifting orbital degeneracy. In the W-doped compound (Fig. 8(c) and (d)), the total DOS near the E_F increases compared to the undoped alloy, reflecting enhanced electronic instability in the cubic phase and a stronger driving force toward martensite formation. This finding is consistent with the results of Gamzatov et al. [57], who

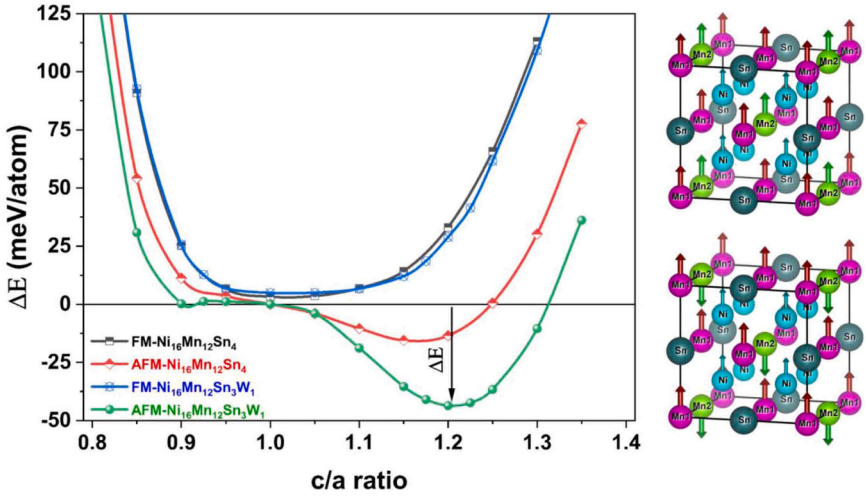

Fig. 7. Dependence of the total energy as a function of tetragonal ratio (c/a) for $Ni_{16}Mn_{12}Sn_{4-x}W_x$ ($x = 0$ and 1) compounds with different magnetic configurations. Mn_1 atoms in the $L2_1$ ordered structure occupy the regular Mn sites, whereas Mn_2 atoms (excess Mn) are located at the Sn sites. The arrows in the crystallographic unit cells indicate the orientation of the magnetic moments, which are mainly located on the Mn atoms.

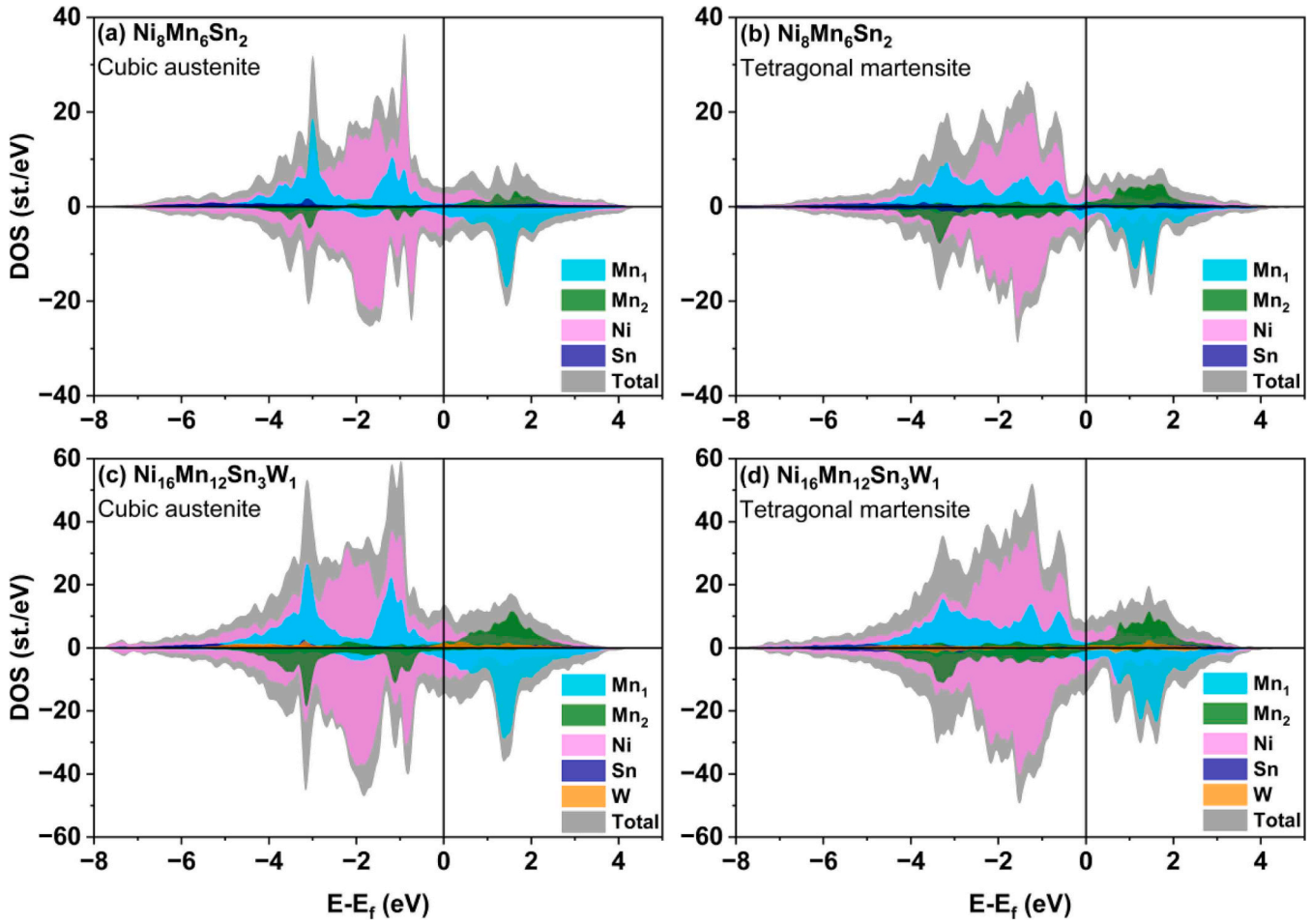

Fig. 8. The spin-resolved total and local density of states (LDOS) for cubic austenite $Ni_8Mn_6Sn_2$ (a), tetragonal martensite $Ni_8Mn_6Sn_2$ (b), cubic austenite $Ni_{16}Mn_{12}Sn_3W_1$ (c), and tetragonal martensite $Ni_{16}Mn_{12}Sn_3W_1$ (d) compounds.

reported that a higher DOS at the Fermi level correlates with reduced structural stability and an increased MT temperature. These results further support the conclusion that W-doping increases the thermodynamic driving force that stabilizes the tetragonal phase over the cubic phase, thereby shifting the transition to higher temperatures.

Fig. 9 displays the spin-resolved DOS projected onto the *d*-orbitals (t_{2g}, e_g) of Ni, Mn, and W for both cubic and tetragonal phases of undoped and W-doped Ni–Mn–Sn Heusler-type alloys. In the cubic $L2_1$ structure (Fig. 9(a)), the minority-spin valence band exhibits pronounced hybridization between Mn_1 t_{2g} and Ni e_g, states within the energy range of –4 to –0.5 eV. The minority-spin channel near the Fermi level is primarily characterized by Ni e_g states, with comparatively weaker contributions from Mn_1. Following tetragonal distortion (Fig. 9 (b)), the Ni e_g peak undergoes splitting, and the Mn_1 t_{2g} features shift toward lower energies, which reduces degeneracy and stabilizes the martensitic phase. This behavior clearly demonstrates the Jahn–Teller effect at the *d*-orbital level [57,58].

Fig. 9(c) and (d) additional 5*d* states originating from W interact with Ni and Mn *d*-orbitals, thereby intensifying hybridization in the case of the W-doped compound. This increased hybridization alters the electronic structure by broadening the DOS and increasing the spectral weight at the Fermi level, thereby reducing cubic stability and enhancing the MT temperature. Additionally, the W dopant introduces additional valence electrons, increasing the *e*/a ratio and modifying lattice parameters, which correlates with a higher martensitic transformation temperature and improved magnetocaloric performance.

Fig. 10 illustrates the spin-resolved density of states (DOS) for the Sn 5*p* orbitals and their hybridization with the W 5*d* orbitals in $Ni_{16}Mn_{12}Sn_3W_1$ compounds, comparing the cubic austenite and tetragonal martensite phases. Fig. 10 (a–c) corresponds to the cubic phase, showing Sn $5p_x$, $5p_y$, and $5p_z$ interactions with W $5d_{xy}$, $5d_{yz}$, $5d_{xz}$, $5d^2_{x^2-y^2}$, and $5d^2_z$. Fig. (d–f) depicts the same hybridization in the martensitic phase.

From a quantum-mechanical perspective, hybridization between the Sn 5*p* and W 5*d* orbitals is allowed because they are close in energy and both are spatially extended, thereby facilitating strong overlap. Therefore, the W element, as a 5*d* element, has more delocalized and broader orbitals than 3*d* or 4*d* elements, which significantly enhances *p*-*d* hybridization. Symmetry considerations indicate that Sn $5p_x$ primarily hybridizes with W $5d_{xy}$, $5d_{zx}$, and $5d^2_{x^2-y^2}$, Sn $5p_y$ with W $5d_{xy}$, $5d_{yz}$, and $5d^2_{x^2-y^2}$, and Sn $5p_z$ strongly with W $5d_{yz}$, $5d_{zx}$, and $5d^2_z$.The strong overlap between Sn $5p_z$ and $5d^2_z$ orbitals is evident in the partial DOS, indicating enhanced covalent bonding that broadens Sn *p*-states near the Fermi level, reduces electronic localization, and destabilizes the cubic structure, thereby promoting the martensitic transformation. Furthermore, Entel et al. [59] highlight that symmetrical breaking and orbital hybridization are fundamental drivers of phase stability in Ni_2MnGa Heusler-type alloys. These findings confirm that W-doping significantly strengthens *p*–*d* hybridization compared to undoped alloys, consistent with previous studies on Ni–Mn–Z Heusler-type alloys [15,60].

4. Conclusions

This work demonstrates that W-doping is an effective strategy for tailoring the martensitic transformation (MT) and magnetocaloric performance of Ni–Mn–Sn metamagnetic shape memory alloys

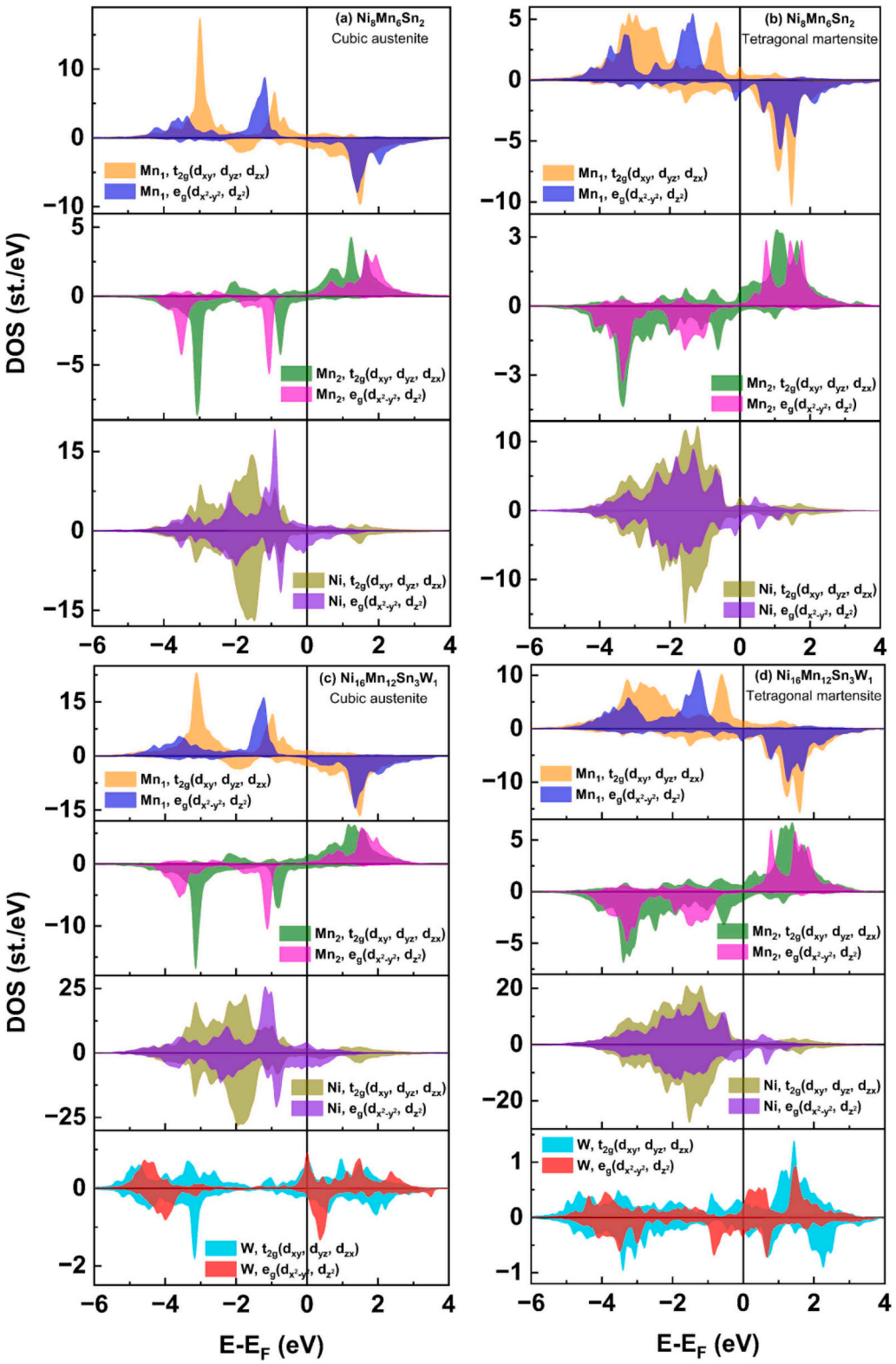

Fig. 9. The *d*-orbital spin-resolved density of states (DOS) for Mn, Ni, and W of (a) cubic austenite $Ni_8Mn_6Sn_2$, (b) tetragonal martensite $Ni_8Mn_6Sn_2$, (c) cubic austenite $Ni_{16}Mn_{12}Sn_3W_1$, and (d) tetragonal martensite $Ni_{16}Mn_{12}Sn_3W_1$ compounds.

(MetaMSMAs). Through a combined experimental and computational study of $Ni_{47}Mn_{40}Sn_{13-x}W_x$ (x=0, 0.5, 1, and 1.25 at%) MetaMSMA, we found that substituting Sn with W systematically shifts MT toward room temperature, enhances the inverse magnetocaloric effect (MCE), and improves its cyclic stability due to reduced thermal hysteresis.

X-ray diffraction analysis confirms the presence of the $L2_1$ austenitic structure for $x = 0$, 0.5, and 1 and an orthorhombic martensite phase at $x = 1.25$, which is consistent with the gradual stabilization of the low-symmetry martensitic phase as x increases. The unit cell volume decreases upon replacing Sn with W in Ni–Mn–Sn MetaMSMAs; however, in conjunction with the e/a parameter, it plays an important role in increasing the MT temperature.

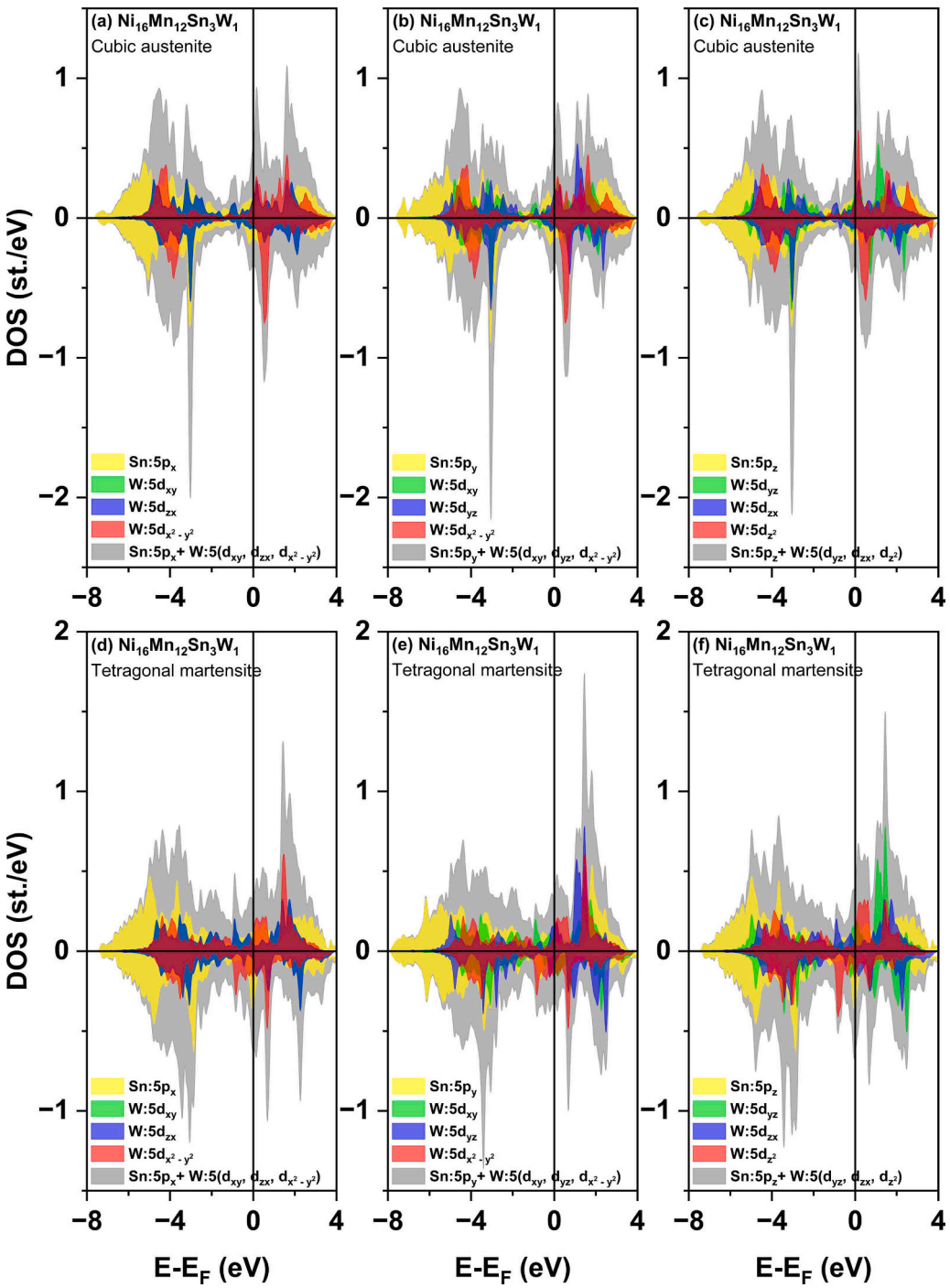

Fig. 10. The spin-resolved density of states (DOS) of *p-d* hybridization for Sn and W in the $Ni_{16}Mn_{12}Sn_3W_1$ compound: (a) Sn $5p_x$ with W $5d_{xy}$, $5d_{zx}$, and $5d^2_{x\,y}$, (b) Sn $5p_y$ with W $5d_{xy}$, $5d_{yz}$, and $5d^2_{x\,y}$, (c) Sn $5p_z$ with W $5d_{yz}$, $5d_{zx}$, and $5d^2_z$ in cubic austenite state. (d) Sn $5p_x$ with W $5d_{xy}$, $5d_{zx}$, and $5d^2_{x\,y}$, (e) Sn $5p_y$ with W $5d_{xy}$, $5d_{yz}$, and $5d^2_{x\,y}$, (f) Sn $5p_z$ with W $5d_{yz}$, $5d_{zx}$, and $5d^2_z$ in tetragonal martensite state.

The thermomagnetic data have shown that the field sensitivity of the reverse MT ($\Delta T_A/\mu_0\Delta H$) decreases as the concentration of the W dopant increases. The analysis of these data using the Maxwell relationship revealed that the W-doped alloys exhibit a rise in the magnetic entropy change, ΔS_{iso}, with a peak of 13.2 J/kg·K at 5 T for x = 1 at room temperature, which aligns with MT. The increase in the transformation-induced entropy change, ΔS_{tr}, estimated using the Clausius–Clapeyron equation, supports this improvement and highlights the beneficial relationship between a significant magnetization jump (ΔM), reduced $\Delta T_A/\mu_0\Delta H$, and optimized hysteresis. Although higher fields and larger ΔM initially lead to an increase in MCE, the MCE response eventually tends to saturate as the opposing magnetic entropy effect becomes more significant. This outcome emphasizes the trade-off inherent in inverse magnetocaloric effect systems and highlights the need to balance the ΔM value and field-induced shift of MT in order to achieve optimal refrigeration performance.

Direct cycling measurements of the $x = 1$ alloy using an adiabatic magnetocalorimeter show that the ΔT_{ad} values for the first-order martensitic transition (FOMT) and the second-order magnetic transition (SOMT) remain stable at 0.5 K and 1.4 K, respectively, during repeated cycling at a magnetic field of 1.96 T. Such stability justifies the practical potential of the $x = 1$ alloy for magnetic refrigeration at near

room temperature. This performance is significantly better than that of the rapid inverse–direct crossover observed in related Ni–Mn–based systems, which exhibit broader hysteresis. Near Curie temperatures, the SOMT shows smooth and reversible behavior over hundreds of cycles, thus confirming reliable operation in both the FOMT and SOMT modes.

Density functional theory calculations using supercells replicate the experimental finding that W-doping stabilizes the tetragonal martensitic phase by increasing the energy gap between the cubic and tetragonal states (from approximately 15.824 meV to 43.636 meV per formula unit), which qualitatively correlates with the observed increase in the MT temperature. Analyses of the total and local density of states (LDOS) indicate that the W element, as a nonmagnetic 5*d* dopant, reduces the ferromagnetic exchange coupling by promoting antiferromagnetic Mn_1-Mn_2 alignment and increases the DOS near the Fermi level. Notably, the W dopant enhances the *p*–*d* hybridization between the Ni 3*d*, Mn 3*d*, and Sn 5*p* orbitals, leading to an intensification of the Jahn–Teller-type band splitting in the martensitic phase and amplification of the electronic instability of the cubic phase. Thus, this effect increases the driving force that stabilizes the tetragonal phase. These results demonstrate that modest increases in the *e*/a ratio, combined with targeted changes in lattice contraction and hybridization, account for the experimentally observed rise in MT temperature and improved magnetocaloric performance.

In summary, by combining structural, magnetic, magnetocaloric, and electronic approaches, it was found that careful selection of fourth-element transition-metal doping (specifically tungsten) provides a precise tool to co-optimize the MT location, hysteresis width, and entropy balance. In addition, the established *p*–*d* hybridization framework, which involves Ni 3*d* and Mn 3*d*/Sn 2*p* states enhanced by a 5*d* dopant, facilitates more accurate theoretical design and predictive tuning within the broader family of Ni–Mn–Z Heusler-type alloys. It was proved that W-doping Ni–Mn–Sn MetaMSMAs offers a desirable combination of adjustable MT temperature, high ΔS_{iso}, and stable ΔT_{ad} during cycling, making them promising materials as promising materials for magnetic refrigeration applications.

CRediT authorship contribution statement

Meysam Norouzi-Inallu: Conceptualization, Data curation, Formal analysis, Funding acquisition, Investigation, Methodology, Project administration, Resources, Software, Supervision, Validation, Visualization, Writing – original draft, Writing – review & editing. **Ali Ghotbi Varzaneh:** Conceptualization, Data curation, Formal analysis, Funding acquisition, Investigation, Methodology, Project administration, Resources, Software, Supervision, Writing – review & editing. **Parviz Kameli:** Funding acquisition, Supervision, Writing – review & editing. **Ismaeil Abdolhosseini Sarsari:** Project administration, Software, Writing – review & editing. **Taghi Amiri:** Resources. **Masoud Moshtaghi:** Funding acquisition, Supervision, Writing – review & editing. **Jingyuan Xu:** Writing – review & editing. **Volodymyr Chernenko:** Supervision, Writing – review & editing. **Daniel Salazar:** Funding acquisition, Writing – review & editing. **Manfred Kohl:** Supervision.

Declaration of Generative AI and AI-assisted technologies in the writing process

During the preparation of this work, the authors used Grammarly, Copilot, and ChatGPT in order to enhance the fluency and coherence of the text. After using these tools, the authors reviewed and edited the content as needed and take full responsibility for the content of the publication.

Declaration of Competing Interest

The authors declare that they have no known competing financial interests or personal relationships that could have appeared to influence the work reported in this paper.

Acknowledgments

M. Nourozi-Inallu acknowledges funding from the Finnish Academy of Science and Letters (Väisälä Fund), the Erasmus + staff mobility grant of LUT University (projects 23B30953YT40 and 23B30961YT40), and the Research Council of Finland (project number: 370633). A.G Varzaneh acknowledges funding from the Alexander von Humboldt Foundation. D. Salazar acknowledges funding from the Basque Government Department of Education (projects KK−2025/00034 and IKUR-QT−3), the Spanish Ministry of Science and Innovation (grant PID2022–138256NA-C22, funded by MCIN/AEI/10.13039/501100011033), and the European Space Agency (grant 4000148229/2025/NL/GLC, WISH Project).

Data availability

Data will be made available on request.

References

[1] A.G. Varzaneh, P. Kameli, I.A. Sarsari, M.G. Zavareh, C.S. Mejía, T. Amiri, Y. Skourski, J.L. Luo, T.H. Etsell, V.A. Chernenko, Magnetic and magnetocaloric properties of Ni 47 Mn 40 Sn 13− x Zn x alloys: direct measurements and first-principles calculations, Phys. Rev. B 101 (2020) 134403.
[2] S.E. Muthu, S. Singh, R. Thiyagarajan, G.K. Selvan, N.V.R. Rao, M.M. Raja, S. Arumugam, Influence of Si substitution on the structure, magnetism, exchange bias and negative magnetoresistance in Ni48Mn39Sn13 Heusler alloys, J. Phys. D. Appl. Phys. 46 (2013) 205001.
[3] P. Lázpita, V.A. L'vov, J.R. Fernández, J.M. Barandiarán, V.A. Chernenko, Combined effect of magnetic field and hydrostatic pressure on the phase transitions exhibited by Ni-Mn-In metamagnetic shape memory alloy, Acta Mater. 193 (2020) 1–9.
[4] V. Franco, J.S. Blázquez, J.J. Ipus, J.Y. Law, L.M. Moreno-Ramírez, A. Conde, Magnetocaloric effect: From materials research to refrigeration devices, Prog. Mater. Sci. 93 (2018) 112–232.
[5] A. Çakır, M. Acet, M. Farle, Exchange bias caused by field-induced spin reconfiguration in Ni-Mn-Sn, Phys. Rev. B 93 (2016) 094411.
[6] E. Villa, F. Villa, B.R. Crespo, P. Lazpita, D. Salazar, H. Hosoda, V. Chernenko, Shape memory and elastocaloric properties of melt-spun NiMn-based Heusler alloys, J. Alloy. Compd. 965 (2023) 171437, https://doi.org/10.1016/j.jallcom.2023.171437.
[7] B. Rodríguez-Crespo, D. Salazar, S. Lanceros-Méndez, V. Chernenko, Development and magnetocaloric properties of Ni(Co)-Mn-Sn printing ink, J. Alloy. Compd. 917 (2022) 165521, https://doi.org/10.1016/j.jallcom.2022.165521.
[8] M. Norouzi-Inallu, V. Laitinen, I. Poutiainen, K. Ullakko, Development of a build volume reduction kit for studying epitaxial re-solidification in laser powder bed fusion, IOP Conf. Ser. Mater. Sci. Eng. 1296 (2023) 012018, https://doi.org/10.1088/1757-899X/1296/1/012018.
[9] M. Fang, F. Tian, K. Cao, X. Ke, Y. Zhang, S. Yang, W. Zuo, Y. Liu, T. Ma, X. Song, Y. Ji, X. Ren, Understanding of the giant magnetic entropy change around the co-occurrence point of martensitic and magnetic transitions in Ni-Mn-In Heusler alloy, Acta Mater. 229 (2022) 117839, https://doi.org/10.1016/J.ACTAMAT.2022.117839.
[10] M. Ye, A. Kimura, Y. Miura, M. Shirai, Y.T. Cui, K. Shimada, H. Namatame, M. Taniguchi, S. Ueda, K. Kobayashi, Role of Electronic Structure in the Martensitic Phase Transition of Ni 2 Mn 1+ x Sn 1-x Studied by Hard-X-Ray Photoelectron Spectroscopy and Ab Initio Calculation, Phys. Rev. Lett. 104 (2010) 176401.
[11] M. Norouzi-Inallu, M. Jafari, D. Salazar, I. Orue, Study of structure, phase transformations, magnetocaloric effect, and critical behavior in Ni51-xFexMn28Ga21 magnetic shape memory alloys, J. Alloy. Compd. 1065 (2026) 188247, https://doi.org/10.1016/J.JALLCOM.2026.188247.
[12] Z. Ghazinezhad, P. Kameli, A. Ghotbi Varzaneh, I.A. Sarsari, M. Norouzi-Inallu, T. Amiri, D. Salazar, B. Rodríguez-Crespo, D. Vashaee, T.H. Etsell, V. Chernenko, Cd-doping effects in Ni–Mn–Sn: experiment and ab-initio study, J. Phys. D. Appl. Phys. 55 (2022) 255001, https://doi.org/10.1088/1361-6463/ac5f33.
[13] V.D. Buchelnikov, V.V. Sokolovskiy, Magnetocaloric effect in Ni-Mn-X (X = Ga, In, Sn, Sb) Heusler alloys, Phys. Met. Metallogr. 112 (2011) 633–665, https://doi.org/10.1134/S0031918X11070052.
[14] A. Pérez-Checa, J.M. Porro, J. Feuchtwanger, P. Lázpita, T.C. Hansen, C. Mondelli, A. Sozinov, J.M. Barandiarán, K. Ullakko, V. Chernenko, Role of Fe addition in Ni–Mn–Ga–Co–Cu–Fe ferromagnetic shape memory alloys for high-temperature magnetic actuation, Acta Mater. 196 (2020) 549–555.
[15] J. Sannigrahi, S. Pramanick, S. Chatterjee, J.S. Lord, D. Khalyavin, A.D. Hillier, D. T. Adroja, S. Majumdar, Magnetic states of Ni-Mn-Sn based shape memory alloy: a combined muon spin relaxation and neutron diffraction study, Phys. Rev. B 99 (2019) 224401.

[16] K.R. Priolkar, P.A. Bhobe, D.N. Lobo, S.W. D'Souza, S.R. Barman, A. Chakrabarti, S. Emura, Antiferromagnetic exchange interactions in the Ni 2 Mn 1.4 In 0.6 ferromagnetic Heusler alloy, Phys. Rev. BCondens. Matter Mater. Phys. 87 (2013) 144412.

[17] V.V. Sokolovskiy, V.D. Buchelnikov, M.A. Zagrebin, P. Entel, S. Sahoo, M. Ogura, First-principles investigation of chemical and structural disorder in magnetic Ni 2 Mn 1+ x Sn 1− x Heusler alloys, Phys. Rev. BCondens. Matter Mater. Phys. 86 (2012) 134418.

[18] K.P. Bhatti, S. El-Khatib, V. Srivastava, R.D. James, C. Leighton, Small-angle neutron scattering study of magnetic ordering and inhomogeneity across the martensitic phase transformation in Ni 50− x Co x Mn 40 Sn 10 alloys, Phys. Rev. B 85 (2012) 134450.

[19] C.O. Aguilar-Ortiz, D. Soto-Parra, P. Álvarez-Alonso, P. Lázpita, D. Salazar, P. O. Castillo-Villa, H. Flores-Zúñiga, V.A. Chernenko, Influence of Fe doping and magnetic field on martensitic transition in Ni–Mn–Sn melt-spun ribbons, Acta Mater. 107 (2016) 9–16.

[20] B. Rodríguez-Crespo, N.A. Río-López, P. Lázpita, S. Ceballos, M. Ríos, D. Domenech, J.A. Rodriguez-Velamazán, J. López-García, V. Chernenko, J. M. Porro, D. Salazar, Impact of magnetic, atomic and microstructural ordering on the magnetocaloric performance of powdered NiCoMnSn metamagnetic shape memory ribbons, Mater. Des. 245 (2024) 113279, https://doi.org/10.1016/j.matdes.2024.113279.

[21] M.N. Inallu, P. Kameli, A.G. Varzaneh, I.A. Sarsari, D. Salazar, I. Orue, V. A. Chernenko, Magnetocaloric effect in W-doped Ni–Mn–Sn alloy probed by direct and indirect measurements, J. Phys. D. Appl. Phys. 52 (2019) 235001.

[22] P. Lázpita, M. Sasmaz, E. Cesari, J.M. Barandiarán, J. Gutiérrez, V.A. Chernenko, Martensitic transformation and magnetic field induced effects in Ni42Co8Mn39Sn11 metamagnetic shape memory alloy, Acta Mater. 109 (2016) 170–176.

[23] M. Norouzi-Inallu, A. Ghotbi Varzaneh, P. Kameli, J. Xu, K. Ullakko, V. Chernenko, H. Hosoda, D. Salazar, Transformation behavior and inverse magnetocaloric effect in Ni45Co5Mn36.7In13.3-xGex melt-spun ribbons, Intermet. (Barking) 165 (2024) 108152, https://doi.org/10.1016/J.INTERMET.2023.108152.

[24] A. Taubel, B. Beckmann, L. Pfeuffer, N. Fortunato, F. Scheibel, S. Ener, T. Gottschall, K.P. Skokov, H. Zhang, O. Gutfleisch, Tailoring magnetocaloric effect in all-d-metal Ni-Co-Mn-Ti Heusler alloys: a combined experimental and theoretical study, Acta Mater. 201 (2020) 425–434, https://doi.org/10.1016/J.ACTAMAT.2020.10.013.

[25] M. Norouzi-Inallu, P. Kameli, A.G. Varzaneh, I.A. Sarsari, M.A. Eskandari, I. Orue, B. Rodríguez-Crespo, V. Chernenko, Influence of W doping on the structure, magnetism and exchange bias in Ni47Mn40Sn13− x W x Heusler alloys, J. Phys. Condens. Matter 34 (2022) 225803.

[26] P. Álvarez-Alonso, J. López-García, G. Daniel-Perez, D. Salazar, P. Lázpita, J. P. Camarillo, H. Flores-Zuñiga, D. Rios-Jara, J.L. Sánchez-Llamazares, V. A. Chernenko, Simple Set-Up for Adiabatic Measurements of Magnetocaloric Effect, Key Eng. Mater. 644 (2015) 215–218, https://doi.org/10.4028/www.scientific.net/KEM.644.215.

[27] K.F. Garrity, J.W. Bennett, K.M. Rabe, D. Vanderbilt, Pseudopotentials for high-throughput DFT calculations, Comput. Mater. Sci. 81 (2014) 446–452.

[28] J.P. Perdew, K. Burke, M. Ernzerhof, Generalized gradient approximation made simple, Phys. Rev. Lett. 77 (1996) 3865.

[29] K. Momma, F. Izumi, VESTA 3 for three-dimensional visualization of crystal, volumetric and morphology data, J. Appl. Crystallogr. 44 (2011) 1272–1276.

[30] A.G. Varzaneh, P. Kameli, T. Amiri, K.K. Ramachandran, A. Mar, I.A. Sarsari, J. L. Luo, T.H. Etsell, H. Salamati, Effect of Cu substitution on magnetocaloric and critical behavior in Ni47Mn40Sn13− xCux alloys, J. Alloy. Compd. 708 (2017) 34–42.

[31] M. Norouzi-Inallu, V. Laitinen, M. Vinogradova, A. Kumthekar, K. Ullakko, Solidification of Ni-Mn-Ga magnetic shape memory alloy built via laser powder bed fusion on a single crystal substrate, J. Alloy. Compd. (2024) 174907.

[32] M. Norouzi-Inallu, I. Poutiainen, K. Ullakko, Study of the wall thickness effect on the solidification and mechanical properties of thin-walled SS316L built via LPBF additive manufacturing, CIRP J. Manuf. Sci. Technol. 61 (2025) 542–553, https://doi.org/10.1016/J.CIRPJ.2025.07.008.

[33] M. Norouzi-Inallu, V. Laitinen, I. Orue, K. Ullakko, Influence of laser powder bed fusion scanning strategies on microstructure, transformation, and magnetic behavior of Ni-Mn-Ga magnetic shape memory alloys, J. Alloy. Compd. 1047 (2025) 185011, https://doi.org/10.1016/J.JALLCOM.2025.185011.

[34] M. Norouzi-Inallu, V. Laitinen, I. Orue, K. Ullakko, Characterization of structural and magnetic phase transformations in Ni-Mn-Ga magnetic shape memory alloys built via laser powder bed fusion, IOP Conf. Ser. Mater. Sci. Eng. 1332 (2025) 012005, https://doi.org/10.1088/1757-899X/1332/1/012005.

[35] G. Porcari, F. Cugini, S. Fabbrici, C. Pernechele, F. Albertini, M. Buzzi, M. Mangia, M. Solzi, Convergence of direct and indirect methods in the magnetocaloric study of first order transformations: The case of Ni-Co-Mn-Ga Heusler alloys, Phys. Rev. B 86 (2012) 104432.

[36] A.G. Gamzatov, A.M. Aliev, A. Ghotbi Varzaneh, P. Kameli, I. Abdolhosseini Sarsari, S.C. Yu, Inverse-direct magnetocaloric effect crossover in Ni47Mn40Sn12.5Cu0. 5 Heusler alloy in cyclic magnetic fields, Appl. Phys. Lett. 113 (2018) 172406.

[37] A.G. Varzaneh, P. Kameli, M. Ríos, B. Aslibeiki, I. Orue, T. Sarkar, V. Chernenko, M. Kohl, J. Xu, D. Salazar, Tailoring Ni–Co–Mn–Sn Ribbons by Ge Doping for Enhanced Magnetocaloric Effect, Adv. Electron. Mater. n/a (n.d.) e00596. https://doi.org/10.1002/aelm.202500596.

[38] W. Ito, Y. Imano, R. Kainuma, Y. Sutou, K. Oikawa, K. Ishida, Martensitic and magnetic transformation behaviors in Heusler-type NiMnIn and NiCoMnIn metamagnetic shape memory alloys, Metall. Mater. Trans. A Phys. Metall. Mater. Sci. (2007) 759–766, https://doi.org/10.1007/s11661-007-9094-9.

[39] J. Liu, T. Gottschall, K.P. Skokov, J.D. Moore, O. Gutfleisch, Giant magnetocaloric effect driven by structural transitions, Nat. Mater. 11 (2012) 620–626.

[40] K. Xu, Z. Li, Y.L. Zhang, C. Jing, An indirect approach based on Clausius–Clapeyron equation to determine entropy change for the first-order magnetocaloric materials, Phys. Lett. A 379 (2015) 3149–3154, https://doi.org/10.1016/J.PHYSLETA.2015.10.029.

[41] S. Ghosh, S. Sangwan, S. Mandal, S. Datta, M. Kar, P. Singh, T.K. Nath, Room temperature giant magneto-caloric effect in Ni45Mn44Sn11-XInX (X = 1, 3) disordered Heusler alloy: The role of martensite transition, J. Magn. Magn. Mater. 562 (2022), https://doi.org/10.1016/j.jmmm.2022.169797.

[42] Y.S. Koshkid'ko, E.T. Dilmieva, A.P. Kamantsev, J. Cwik, K. Rogacki, A. V. Mashirov, V.V. Khovaylo, C.S. Mejia, M.A. Zagrebin, V.V. Sokolovskiy, Magnetocaloric effect and magnetic phase diagram of Ni-Mn-Ga Heusler alloy in steady and pulsed magnetic fields, J. Alloy. Compd. 904 (2022) 164051.

[43] Y.S. Koshkid'ko, E.T. Dilmieva, J. Cwik, K. Rogacki, D. Kowalska, A.P. Kamantsev, V.V. Koledov, A.V. Mashirov, V.G. Shavrov, V.I. Valkov, Giant reversible adiabatic temperature change and isothermal heat transfer of MnAs single crystals studied by direct method in high magnetic fields, J. Alloy. Compd. 798 (2019) 810–819.

[44] A.P. Kamantsev, Y.S. Koshkidko, E.O. Bykov, T. Gottschall, A.G. Gamzatov, A. M. Aliev, A.G. Varzaneh, P. Kameli, Giant irreversibility of the inverse magnetocaloric effect in the Ni47Mn40Sn12. 5Cu0. 5 Heusler alloy, Appl. Phys. Lett. 123 (2023).

[45] A.G. Gamzatov, A.B. Batdalov, S.K. Khizriev, A.M. Aliev, A.G. Varzaneh, P. Kameli, The nature of the frequency dependence of the adiabatic temperature change in Ni50Mn28Ga22-x (Cu, Zn) x Heusler alloys in cyclic magnetic fields, J. Alloy. Compd. 965 (2023) 171451.

[46] E. Stevens, K. Kimes, D. Salazar, A. Mostafaei, R. Rodriguez, A. Acierno, P. Lázpita, V. Chernenko, M. Chmielus, Mastering a 1.2 K hysteresis for martensitic para-ferromagnetic partial transformation in Ni-Mn (Cu)-Ga magnetocaloric material via binder jet 3D printing, Addit. Manuf. 37 (2021) 101560.

[47] P. Álvarez-Alonso, J.P. Camarillo-García, D. Salazar, J. López-García, C. Echevarria-Bonet, P. Lázpita, K. Padrón-Alemán, J.L. Sánchez Llamazares, H. Flores-Zúñiga, V. Chernenko, Investigating the reversible nature of the magnetocaloric effect under cyclic conditions of the Ni50Mn34In15Ga1 magnetic shape memory alloy, J. Alloy. Compd. 993 (2024) 174576, https://doi.org/10.1016/J.JALLCOM.2024.174576.

[48] T. Gottschall, K.P. Skokov, F. Scheibel, M. Acet, M.G. Zavareh, Y. Skourski, J. Wosnitza, M. Farle, O. Gutfleisch, Dynamical effects of the martensitic transition in magnetocaloric heusler alloys from direct Δ T ad measurements under different magnetic-field-sweep rates, Phys. Rev. Appl. 5 (2016) 024013.

[49] P. Álvarez-Alonso, J.P. Camarillo-García, D. Salazar, J. López-García, C. Echevarria-Bonet, P. Lázpita, K. Padrón-Alemán, J.L.S. Llamazares, H. Flores-Zúñiga, V. Chernenko, Investigating the reversible nature of the magnetocaloric effect under cyclic conditions of the Ni50Mn34In15Ga1 magnetic shape memory alloy, J. Alloy. Compd. 993 (2024) 174576.

[50] T. Gottschall, K.P. Skokov, B. Frincu, O. Gutfleisch, Large reversible magnetocaloric effect in Ni-Mn-In-Co, Appl. Phys. Lett. 106 (2015) 021901, https://doi.org/10.1063/1.4905371.

[51] M. Zelený, P. Sedlák, O. Heczko, H. Seiner, P. Veřtát, M. Obata, T. Kotani, T. Oda, L. Straka, Effect of electron localization in theoretical design of Ni-Mn-Ga based magnetic shape memory alloys, Mater. Des. 209 (2021) 109917.

[52] M. Zarifi, P. Kameli, A. Ghotbi Varzaneh, E. Hosseini, M. Norouzi-Inallu, M. Abbasi Eskandari, H. Ahmadvand, Anisotropic resistivity and electroresistance in epitaxial La0.3Pr0.4Ca0.3MnO3 thin films, Appl. Phys. A Mater. Sci. Process. 128 (2022), https://doi.org/10.1007/s00339-022-05292-8.

[53] H. Xiao, C. Yang, R. Wang, L. Xu, G. Liu, V.V. Marchenkov, First-principles study of martensitic transformation and magnetic properties of carbon doped Ni–Mn–Sn Heusler alloys, Phys. Lett. A 380 (2016) 3414–3420, https://doi.org/10.1016/J.PHYSLETA.2016.08.008.

[54] K. Zhang, C. Tan, E. Guo, Z. Feng, J. Zhu, Y. Tong, W. Cai, Simultaneous tuning of martensitic transformation behavior, magnetic and mechanical properties in Ni–Mn–Sn magnetic alloy by Cu doping, J. Mater. Chem. C. Mater. 6 (2018) 5228–5238.

[55] A. Kundu, M.E. Gruner, M. Siewert, A. Hucht, P. Entel, S. Ghosh, Interplay of phase sequence and electronic structure in the modulated martensites of Mn 2 NiGa from first-principles calculations, Phys. Rev. B 96 (2017) 64107.

[56] M. Zelený, A. Sozinov, L. Straka, T. Björkman, R.M. Nieminen, First-principles study of Co-and Cu-doped Ni 2 MnGa along the tetragonal deformation path, Phys. Rev. B 89 (2014) 184103.

[57] A.G. Gamzatov, A.B. Batdalov, V.V. Sokolovskiy, A.M. Aliev, L.N. Khanov, A. A. Mukhuchev, K.R. Erager, V.D. Buchelnikov, A.G. Varzaneh, P. Kameli, V. V. Khovaylo, Kinetic and thermophysical properties of Ni47Mn40Sn13 alloy: Insights from experiment and ab initio study, J. Alloy. Compd. 1008 (2024) 176748, https://doi.org/10.1016/J.JALLCOM.2024.176748.

[58] M. Obata, T. Kotani, T. Oda, Intrinsic instability to martensite phases in ferromagnetic shape memory alloy Ni 2 MnGa: Quasiparticle self-consistent GW investigation, Phys. Rev. Mater. 7 (2023) 024413.

[59] P. Entel, V.D. Buchelnikov, V.V. Khovailo, A.T. Zayak, W.A. Adeagbo, M.E. Gruner, H.C. Herper, E.F. Wassermann, Modelling the phase diagram of magnetic shape memory Heusler alloys, J. Phys. D. Appl. Phys. 39 (2006) 865–889, https://doi.org/10.1088/0022-3727/39/5/S13.

[60] Z.Y. Wei, E.K. Liu, J.H. Chen, Y. Li, G.D. Liu, H.Z. Luo, X.K. Xi, H.W. Zhang, W. H. Wang, G.H. Wu, Realization of multifunctional shape-memory ferromagnets in all-d-metal Heusler phases, Appl. Phys. Lett. 107 (2015) 22406.